
LEARNING USER INTERACTION FORCES USING VISION FOR A SOFT FINGER EXOSUIT

A PREPRINT

**Mohamed Irfan Refai^{1,2,*}, Abdulaziz Y. Alkayas^{2,3}, Anup Teejo Mathew³,
Federico Renda³, Thomas George Thuruthel²**

Email: `{*m.i.mohamedrefai}@utwente.nl`

¹Department of Biomechanical Engineering, University of Twente, The Netherlands,

²Department of Computer Science, University College London, The UK,

³Khalifa University, UAE.

August 6, 2025

ABSTRACT

Wearable assistive devices are increasingly becoming softer. Modelling their interface with human tissue is necessary to capture transmission of dynamic assistance. However, their nonlinear and compliant nature makes both physical modeling and embedded sensing challenging. In this paper, we develop a image-based, learning-based framework to estimate distributed contact forces for a finger-exosuit system. We used the SoRoSim toolbox to generate a diverse dataset of exosuit geometries and actuation scenarios for training. The method accurately estimated interaction forces across multiple contact locations from low-resolution grayscale images, was able to generalize to unseen shapes and actuation levels, and remained robust under visual noise and contrast variations. We integrated the model into a feedback controller, and found that the vision-based estimator functions as a surrogate force sensor for closed-loop control. This approach could be used as a non-intrusive alternative for real-time force estimation for exosuits.

Keywords interaction forces · SoRoSim · assistive robotics · vision-based learning

1 Introduction

Activities of the upper extremity such as reaching and grasping offers individuals independence in interacting with the environment in daily life. However, these activities may be impaired due to aging or trauma [Holt et al., 2013, Saes et al., 2022]. Wearable assistive devices or exosuits can offer continuous support as needed for the individual in daily life [Bardi et al., 2022]. Exosuits made of rigid structures allow better interfacing with the fingers and hand, resulting in efficient transmission of assistance to the user [Bardi et al., 2022, Scherb et al., 2023]. However, such exosuits are generally bulky and have a large form factor. Moreover, any misalignment with the finger or wrist joints can result in resistance or inertial effects [Asbeck et al., 2014]. These factors result in user discomfort over time.

Exosuits made from softer materials can be rather lightweight and conform better to the biological joints [Asbeck et al., 2014]. Therefore, they can be more comfortable than rigid exosuits. However, modelling softer exosuits (or robots) can be quite challenging due to their complex dynamics and continuous interactions with the environment [Rus and Tolley, 2015]. Modelling soft exosuit dynamics and interaction forces with the user is necessary to improve efficiency of these systems during long term use [Massardi et al., 2022].

Measuring the forces between an exosuit and the user is generally challenging. Studies have utilized embedded sensing to measure interactions between exosuit and user or a soft robot with its environment. Pressure mats or force sensitive resistors have been used to extrapolate the interaction between the user and the assistive device [Andrikopoulos et al., 2015, Xiloyannis et al., 2019]. Additionally, embedded solutions such as fibre Bragg grating (FBG) sensors [Khan et al., 2017, Bai et al., 2020], optical transducers [Noh et al., 2016], and pressure sensors [Haraguchi et al., 2015]

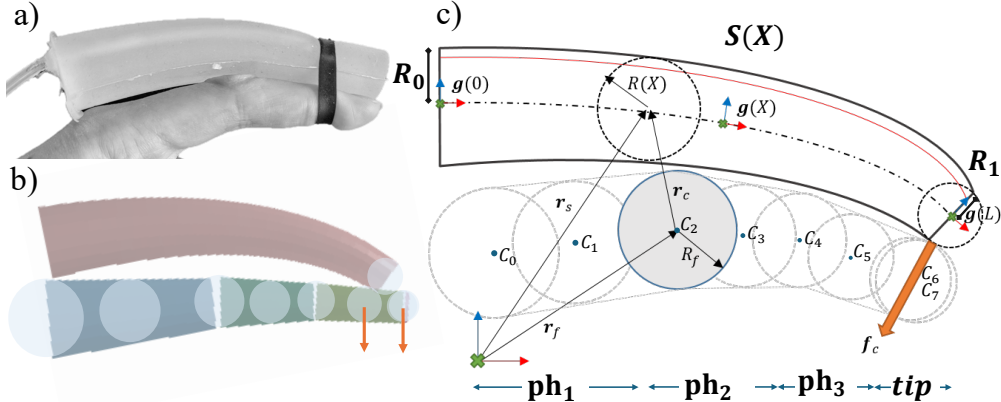


Figure 1: (a) Modelling interaction forces of a soft exosuit using vision-based learning techniques validated using a (b) simulated model. (c) The exosuit is modelled as a Cosserat rod, and the finger as three rigid links connected via rotational joints (RRR). The red line on top of the exosuit shows the line of actuation. Spheres were defined along the exosuit and finger (C_i) to approximate the contact mechanics.

have been previously used for force estimation on soft bodies. However, such methods are highly limited in terms of sensing location, can impede the motion of the soft body, and are not applicable to all design forms.

Alternatively, accurate forward models of soft-bodied systems can be used to estimate interaction forces when combined with optimization techniques. Model-based approaches have been used to estimate external forces from observed states or deformations in soft robotic systems that deform with constant curvature [Camarillo et al., 2008, Gao et al., 2016, Rucker and Webster, 2011, Bajo and Simaan, 2016]. Advanced modelling approaches are however required for state estimation of complex soft-bodied systems without embedded sensors. Although, Finite Element Methods (FEM) can provide a comprehensive analysis of the interaction dynamics between the exosuit and the user [Faure et al., 2012, Ménager et al., 2025], they can be computationally intensive to simulate and optimize. Simplified (In-)Finite Dimensional Models of soft robots offer efficient modelling alternative for interaction and control analyses [Santina et al., 2023, Armanini et al., 2023]. The SoRoSim toolbox [Mathew et al., 2023] implements such an approach to model multibody hybrid structures using the Geometric Variable Strain (GVS) model [Boyer et al., 2020, Renda et al., 2020, Mathew et al., 2024].

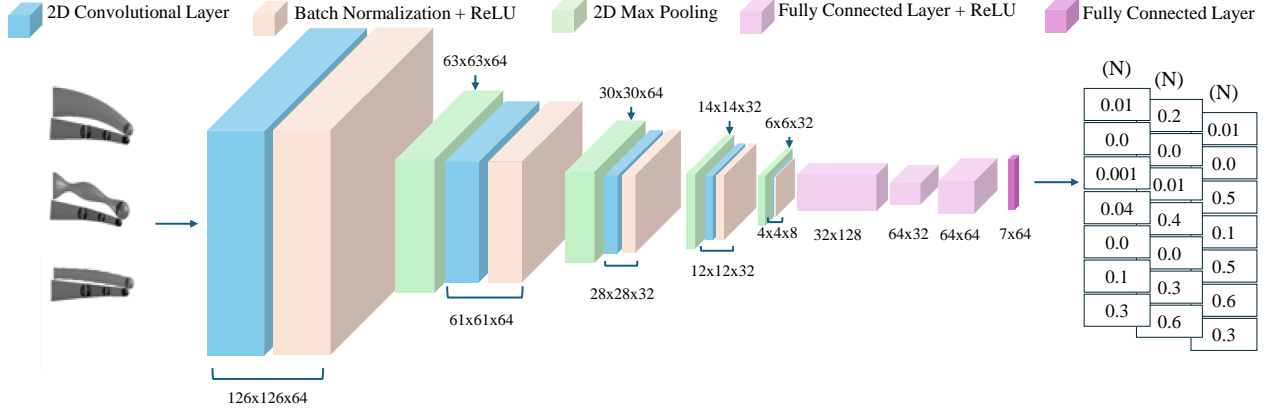
Nonetheless, model-based techniques still require identification of system parameters from real-world data which is challenging for complex nonlinear behaviour of viscoelastic materials. Learning-based techniques have been shown to be successful in abstracting soft-robotics dynamics from images [Monteiro et al., 2023]. In this simulation study, we test whether similar techniques can be applied to our problem. Therefore, we develop a data-driven modelling framework for estimating the interaction forces between a soft exosuit and the finger it is assisting. Our modelling and perception approach relies only on visual data that can be obtained using simple external cameras. The framework is an extension of studies which estimate tip forces [Chen et al., 2024] and soft-bodied deformation [Huang et al., 2024] using convolutional neural networks. Unlike these studies, we show how such data-driven methods can generalize to new shapes and estimate contact forces at multiple locations without any explicit optimization techniques. We validate our model on a finger-exosuit system modelled using the SoRoSim toolbox. The exosuit, composed of a soft, actuated body, facilitates bending of the human finger when actuated. We test the robustness of the technique to varied visual noise and perform further validation on closed-loop control tasks.

2 Methods

Section 2.1 describes the finger-exosuit design. The CNN force estimator architecture is described in Section 2.2, followed by the synthesis of datasets for learning in Section 2.3. We assess the generalizability of the CNN force estimator and use in a feedback controller in Sections 2.4 and 2.5 respectively. Finally, we describe the results presented in Section 2.6.

Table 1: Initial design parameters of the finger-exosuit

Item	Length (cm)	Radius Base (cm)	Radius Tip (cm)	Joint Stiffness (Nm/rad)
exosuit	10	0.58	0.4	–
ph_1	4.5	1.08	0.695	0.04
ph_2	2.53	0.695	0.51	0.03
ph_3	2.36	0.51	0.435	0.02
tip	0.1	0.435	0.4	–

Figure 2: Architecture of the CNN mapping low resolution (128x128) grayscale images of the finger-exosuit system to 1x7 contact forces. The contact forces are measured on C_i , where $i \in \{1, 2, \dots, 7\}$.

2.1 Modelling the finger-exosuit system

Figure 1a depicts the exosuit worn in parallel with the index finger. The finger-exosuit system was modelled using SoRoSim toolbox¹ [Mathew et al., 2023].

2.1.1 Kinematics of the exosuit

The exosuit was designed to simulate a soft body made with silicone, and can be actuated along a line of actuation placed on the surface opposite to the finger. The soft exosuit is modeled as a Cosserat rod, which is a continuum of rigid cross-sections along a curvilinear coordinate $X \in [0, L]$, with L the total length. Each cross-section carries an orthonormal frame, yielding the rod's configuration as a directed spatial curve $\mathbf{g}(X) \in SE(3)$, represented by a homogeneous transformation matrix:

$$\mathbf{g}(X) = \begin{bmatrix} \mathbf{R} & \mathbf{r} \\ \mathbf{0}^{1 \times 3} & 1 \end{bmatrix} \quad (1)$$

where $\mathbf{r}(X) \in \mathbb{R}^3$ is the position of the moving frame's origin, and $\mathbf{R}(X) \in SO(3)$ defines its orientation relative to the spatial frame, with the local x-axis orthogonal to the cross-sectional plane. Differentiating equation (1) with respect to space $(\cdot)'$ and time $(\cdot)'$ gives:

$$\mathbf{g}'(X) = \mathbf{g}\hat{\xi}; \quad \dot{\mathbf{g}}(X) = \mathbf{g}\hat{\eta} \quad (2)$$

The Cosserat rod's strain is denoted by $\hat{\xi}(X)$, and its velocity twist by $\hat{\eta}(X)$, capturing translational and rotational velocities along the rod. The operator $(\hat{\bullet})$ maps \mathbb{R}^6 to $\mathfrak{se}(3)$. Equating mixed partial derivatives in space X and time t reveals the following relationship:

$$\eta' = \dot{\xi} - \text{ad}_{\xi}\eta \quad (3)$$

where ad_{ξ} is the adjoint operator of ξ .

¹<https://github.com/SoRoSim/SoRoSim.git>

The pose model is obtained by integrating eqn. (2), whereas the velocity model is obtained by integrating eqn. (3):

$$\mathbf{g}(X) = \exp\left(\widehat{\boldsymbol{\Omega}}(X)\right), \quad (4)$$

$$\boldsymbol{\eta}(X) = \text{Ad}_{\mathbf{g}^{-1}} \int_0^X \text{Ad}_{\mathbf{g}} \dot{\boldsymbol{\xi}} ds \quad (5)$$

The Adjoint of the homogeneous matrix \mathbf{g} is denoted $\text{Ad}_{\mathbf{g}}$, and the Magnus expansion of $\boldsymbol{\xi}(X)$ by $\boldsymbol{\Omega}$. The generalized coordinates are introduced, and the continuous strain field is discretized using a finite set of strain bases:

$$\boldsymbol{\xi}(X) = \boldsymbol{\Phi}_{\xi}(X)\mathbf{q} + \boldsymbol{\xi}^*(X) \quad (6)$$

Here, $\boldsymbol{\Phi}_{\xi}(X) \in \mathbb{R}^{6 \times n}$ defines the strain basis, $\mathbf{q} \in \mathbb{R}^n$ is the vector of generalized coordinates, and $\boldsymbol{\xi}^*(X)$ denotes the natural (unstressed) strain. Substituting equation (6) into (3) yields the velocity model:

$$\boldsymbol{\eta}(X) = \text{Ad}_{\mathbf{g}(X)}^{-1} \int_0^X \text{Ad}_{\mathbf{g}} \boldsymbol{\Phi}_{\xi} ds \dot{\mathbf{q}} = \mathbf{J}(\mathbf{q}, X) \dot{\mathbf{q}} \quad (7)$$

Here, the geometric Jacobian is represented by $\mathbf{J} \in \mathbb{R}^{6 \times n}$. Despite being analytical, eqns. (4) and (5) cannot be directly calculated. [Mathew et al., 2024, Renda et al., 2022] offers a quadrature approximation of the Magnus expansion $\boldsymbol{\Omega}$ in a recursive formulation of the kinematic equations. The exosuit uses a nodal strain basis akin to the quadratic FEM basis, with three quadrature points [Mathew et al., 2024] allowing degrees of freedom including extension along the local x-axis and bending about the y-axis.

2.1.2 Kinematics of the finger

The finger was modelled as a rigid passive three-bar linkage with rotational joints (RRR) as seen in Table 1. The length of the links (ph_1, ph_2, ph_3) were 4.5, 2.5, and 2.4 cm respectively, and their base radii were 1.1, 0.7, and 0.5 cm respectively [Kuo and Deshpande, 2012]. The stiffness of the joint between the base and ph_1 was 0.04 Nm/rad, and 0.03, and 0.02 Nm/rad respectively for the successive joints [Shi et al., 2020]. The linkage modeling follows classical rigid robot modeling techniques [Lynch and Park, 2017], with external loads defined by contact forces included. Additional contact points at the fingertip were modeled using a fixed link of negligible length.

The full system comprises 25 degrees of freedom: 22 for the exosuit's kinematics and 3 for the finger joint rotations. The rotation of the first finger joint was restricted to the range of -10° to 90° , while the second and third joints were constrained between -5° and 90° .

2.1.3 Contact forces

To simulate exosuit–finger interaction, a simplified interference contact model was used, approximating contact as between two spheres (see Fig. 1). The model is defined as follows:

$$\mathbf{f}_{C_i} = \begin{cases} kd_i \frac{\mathbf{r}_{c_i}}{\|\mathbf{r}_{c_i}\|} & \text{if } d_i > 0 \\ 0 & \text{if } d_i \leq 0 \end{cases}, \quad (8)$$

where $\mathbf{r}_{c_i} = \mathbf{r}_s(X) - \mathbf{r}_{f_i}$, $d_i = R_{f_i} + R(X) - \|\mathbf{r}_{c_i}\|$, and k represents the contact stiffness of the model. The contact force model includes only a normal component, with tangential friction neglected for simplicity. The SoRoSim toolbox identified a total of 42 gaussian quadrature points along the exosuit, each of which had a contact sphere. For the finger, two contact spheres were defined for each rigid link; one at the base and another at the Centre of Mass, resulting in eight contact spheres (C_i , where $i \in \{0, 1, \dots, 7\}$). We found this discretization to be suitable with the limited motion of the rigid bodies. The system's static equilibrium was determined by solving for the contact interactions between the finger and the exosuit.

2.1.4 Statics

The generalized static equation is obtained by projecting the static equilibrium equations of the soft exosuit and the rigid finger onto the space of generalized coordinates using the geometric Jacobian, following D'Alembert's principle [Renda et al., 2020]:

$$\mathbf{K}\mathbf{q} = \mathbf{B}(\mathbf{q})\mathbf{u} + \mathbf{F}(\mathbf{q}). \quad (9)$$

Table 2: Bounds for each parameter

Parameter	Lower Bd.	Upper Bd.	Steps	Eqn.
L	7 cm	11 cm	0.01 cm	—
R_0, R_1	0.4 cm	1 cm	0.01 cm	(10)
A, B	-15	1e-3	0.1	(11), (12)
C, D	1e-4	5	0.01	(13)
m_n	0.001	1	5e-3	(14)

Here, $\mathbf{K} \in \mathbb{R}^{n \times n}$ is the stiffness matrix, $\mathbf{B}(\mathbf{q}) \in \mathbb{R}^n$ is the actuation matrix, u is the pneumatic actuation force (shown as the red line in Fig. 1), and $\mathbf{F}(\mathbf{q}) \in \mathbb{R}^n$ represents generalized external (contact) forces. The Young's modulus was 30 kPa, representing that of Ecoflex.

To solve the full system model, root-finding methods are applied to eqn. (9). The actuation force is incrementally increased, using each equilibrium solution as the initial guess for the next step, ensuring stability and computational efficiency as the load gradually increases.

2.2 CNN Force estimator architecture

The CNN model (Fig. 2) was designed to map the image of the finger-exosuit system with the interaction forces defined along the finger. We employed a single network to estimate the normal forces along the finger at seven predefined points in the simulation. The model must therefore infer the kinemato-static behavior of the soft robot (for any shape) and additionally estimate the contact locations and interaction forces. The model architecture has 5 convolutional layers with 64, 64, 32, 32, and 8 filters respectively, each with a 3x3 kernel. Each of the first four layers were followed with a batch normalization, a ReLU activation, and a 2x2 max pooling layer. Three fully connected layers (32, 32, 64 neurons respectively) were placed next, each with a ReLU activation layer. Finally, a fully connected layer with 64 neurons was mapped to the 1x8 force outputs. C_0 was always 0 and therefore ignored for later analyses. There were a total of 78,847 trainable parameters.

The network utilized an Adam optimizer with an L1 loss function. The batch size was set to 64. The learning rate was initialized to $2e-4$, which was reduced by 0.1 when plateauing (after at least 10 epochs). Training was stopped when validation loss (measured every 5 iterations) did not improve after 5 instances.

Training was done using pytorch library on an Ubuntu system running on Intel(R) Xeon(R) CPU (2.20GHz) with a Titan XP GPU (GP102, NVIDIA, 33MHz clock).

2.3 Simulation of dataset for learning

We generated different exosuit shapes by varying the length L and the shape of the exosuit surface $S(X)$, and actuated them to simulate data for training the CNN. We formulated five different approaches to model $S(X)$ as follows:

$$R_{0,1} : S(X) = R_0 + X_L \cdot (R_1 - R_0), \quad (10)$$

$$R_s : S(X) = R_0 + \frac{R_0}{20} \sin(A \cdot pi \cdot X_L), \quad (11)$$

$$R_{cc} : S(X) = \sum_{n=0}^6 B_n \cos(\pi \cdot n \cdot X_L), \quad (12)$$

$$R_{sc} : S(X) = R_0 + R_s (\sin(C \cdot \pi \cdot X_L + \phi_C) + \cos(D \cdot \pi \cdot X_L + \phi_D)), \quad (13)$$

$$R_{LP} : S(X) = \sum_{n=0}^{N-1} \frac{2m_n}{3^n} P_n(X_L). \quad (14)$$

Eqn. (10) models $S(X)$ linearly from the base (R_0) to tip (R_1) of the exosuit. Here, X_L is the normalized length along the axis of the exosuit. The two parameters (R_0, R_1) can be adjusted to simulate different exosuit shapes. In eqn. (11), the frequency factor A can be varied to generate different exosuit shapes. Eqn. (12) defines the $S(X)$ as a sum of 6 cosine waves, where the amplitude (B_n) of each can be varied. Eqn. (13) formulates $S(X)$ as the sum of a sine and a cosine wave, with four degrees of freedom (frequency (C, D) and phase (ϕ_C, ϕ_D)). Finally, eqn. (14) denotes

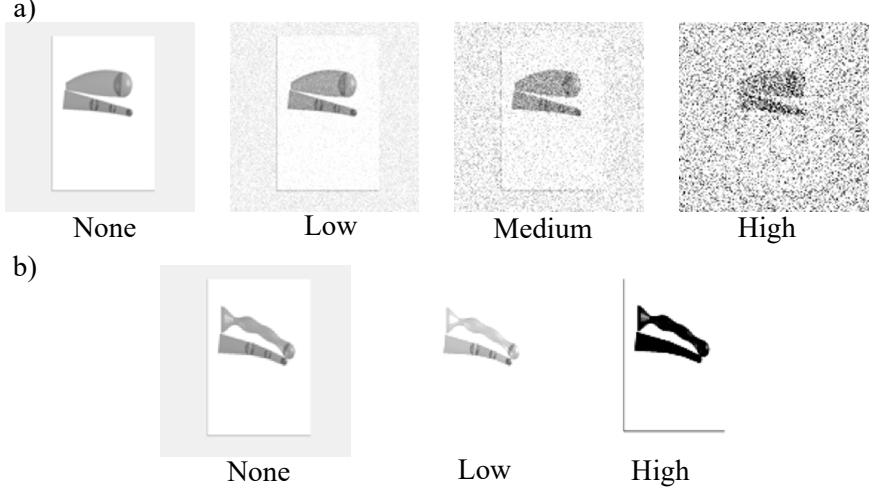


Figure 3: Adulterating the test dataset with (a) gaussian white noise with different variances (Low = 0.001, Medium = 0.01, and High= 0.1) or (b) converted to low or high contrast images.

$S(X)$ as a sum of Legendre Polynomials (LP), where the amplitude of the LPs (m_n) could be varied. To prevent very small exosuit thickness, the minimum radius of the exosuit was limited to 0.4 cm. By combining the $S(X)$ with L , and varying either or both, we had 11 scenarios for simulating a unique exosuit. The bounds of each parameter is mentioned in Table 2. We randomly selected unique combinations from these parameter bounds to generate 125 different instances for each scenario, resulting in 1375 unique exosuit shapes. For each shape, we actuated the finger-exosuit system with force of 0 to 4 N and back to 0 N. From this actuation, we interpolated 50 frames resulting in a total of 68,750 frames. For a few instances, the exosuit reached unrealistic poses after actuation. We filtered the poses where the exosuit tip was below the finger tip, resulting in a total of 65,637 frames of the finger-exosuit system for learning. The simulated frames were then randomized and split into training (60%), validation (20%), and testing (20%) sets. All the results shown in the next section are obtained on the test set.

2.4 Generalizability

The generalizability of the CNN force estimator was assessed by contaminating the test set (Fig. 3). The MATLAB function **imnoise** was used to add gaussian white noise ($\mu = 0.01$) with low, medium, or high variances (0.001, 0.01, and 0.1 respectively) to the frames. We also tested the performance of the CNN force estimator to varying image contrast. The pixel values were mapped from [1, 256] to [26, 200] and [174, 240] respectively for low and high contrast using the MATLAB function **imadjust**.

2.5 Feedback controller embedded with CNN force estimator

The CNN force estimator was integrated as a force sensor within a feedback controller as seen in Fig. 4. For these tests, we defined the $S(X)$ with eqn. (10), with R_0 , R_1 , and L as 1 cm, 0.5 cm, and 9.5 cm respectively. The equations describing the controller are as follows:

$$F_{net} = \sum_{i=1}^7 \|f_{C_i}\|, \text{ and} \quad (15)$$

$$u_k = u_{k-1} + K_P \cdot e_k. \quad (16)$$

The controlled variable was the sum of contact forces (F_{net}) across all spheres on the finger (Fig. 1). The error e_k at step k between the force measured by the CNN force estimator and the target force F_t was implemented in a simple proportional control law to estimate the control input (u_k). u_k was then used to actuate the exosuit. A low-resolution snapshot of the resulting pose ($I_{128 \times 128}$) is then sent to the CNN force estimator to estimate the F_{net} .

The steady-state and step responses were studied. For the steady-state test, three F_t (0.25, 0.3, and 0.35 N) were defined. Here, the controller gain K_P was tuned empirically to 5. For the step response, an input of 0.2 N was provided for 10 s followed by 10 s of 0 N. Here, we tested the responses for $K_P = 0.1, 1$, and 100.

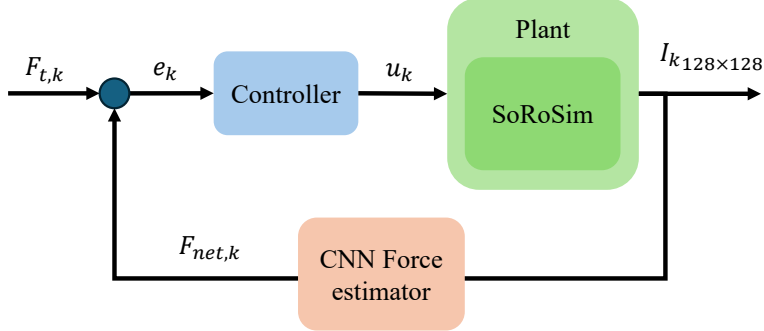


Figure 4: Feedback controller with the CNN force estimator as a force sensor. The target force (F_t) is tracked using a proportional controller, which estimates actuation u for driving the finger-exosuit model in SoRoSim. A low-resolution grayscale snapshot of the resulting pose ($I_{128 \times 128}$) is fed to the CNN force estimator which estimates the contact force at each C_i along the finger, which is summed to get the F_{net} .

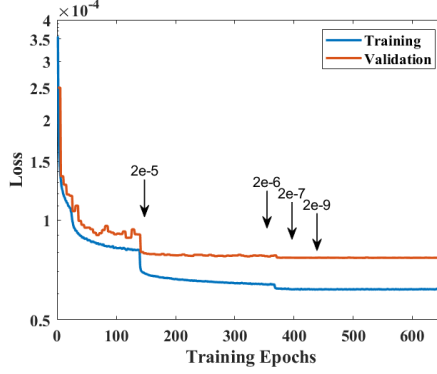


Figure 5: Evolution of the loss functions. The learning rate initialized at $2e - 4$ reduces when plateauing.

Table 3: CNN performance for f_{C_i}

Metric	C_1	C_2	C_3	C_4	C_5	C_6	C_7
RMSE (N)	0.02	0.01	0.06	0.07	0.06	0.07	0.01
RMS%	0.91	0.64	1.6	2.64	3.89	3.85	5.3
CORR	0.92	0.99	0.92	0.82	0.78	0.51	0.93

2.6 Analysis of Results

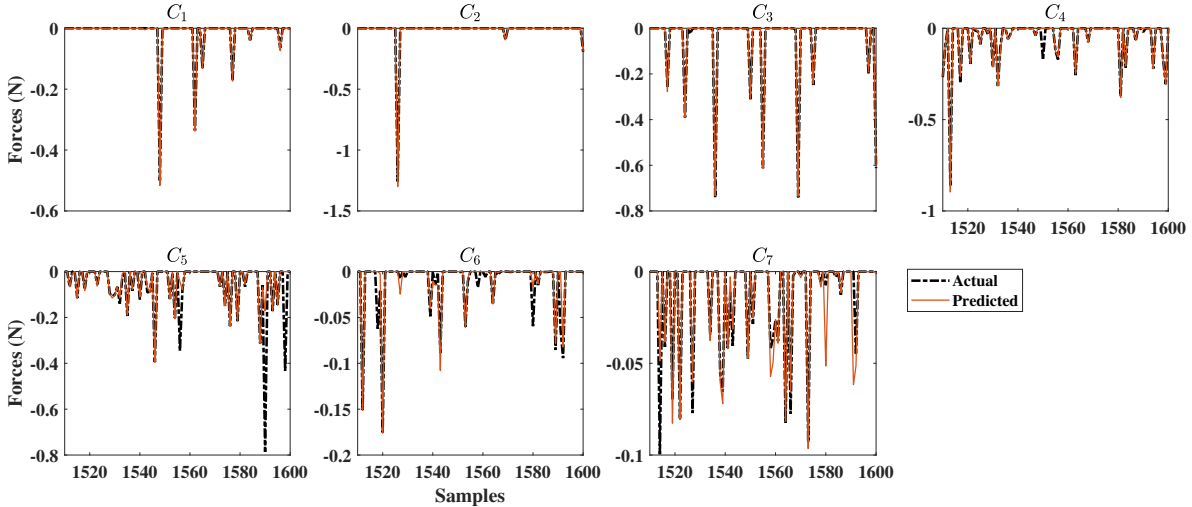
We evaluate and describe the training performance of the CNN, followed by the performance on the test dataset. We show the overall performance using correlation and violin plots [Bechtold, 2016], as well as a sample-by-sample comparison for randomly selected frames. The overall performance is also reported using root mean square of the differences (RMSE) between the predicted and actual force values measured at each C_i . Additionally, we report the RMSE normalized to the range of the target force values (RMS%) and Pearson’s correlation for each C_i . The RMSE, RMS%, and CORR are then reported for the generalizability tests on contaminated images. We compare and discuss the performance of the CNN force estimator for both the steady-state and step responses of the feedback controller. All analyses were performed on MATLAB 2024 (Mathworks MA) running on a 13 Gen Intel PC with 32 RAM with 2.4 GHz. The CNN model was transformed from python to MATLAB using the function `importNetworkFromPyTorch`.

3 Results

The progression of training and validation losses are seen in Fig. 5. The validation loss has saturated after 157 epochs with a slight improvement after 371 epochs when the learning rate was reduced to $2e - 6$. The training stopped at 656 epochs due to no improvement in the validation loss. The training took about 270 minutes.

Table 4: Average performance across C_i for adulterated test images

Metric	None	Low	Medium	High
<i>Gaussian Noise</i>				
RMSE (N)	0.04 ± 0.03	0.05 ± 0.03	0.07 ± 0.03	0.09 ± 0.04
RMS%	2.72 ± 1.78	3.03 ± 2.03	5.14 ± 3.98	6.42 ± 4.65
CORR	0.83 ± 0.16	0.82 ± 0.16	0.56 ± 0.19	0.11 ± 0.07
<i>Contrast</i>				
RMSE (N)	0.04 ± 0.03	0.05 ± 0.03	—	0.08 ± 0.04
RMS%	2.72 ± 1.78	3.58 ± 2.19	—	5.06 ± 2.56
CORR	0.83 ± 0.16	0.78 ± 0.16	—	0.77 ± 0.18

Figure 6: Performance of CNN force estimator for a random set of samples. Each panel compares the prediction of contact force with the actual values measured at C_i with the SoRoSim model.

The performance of the CNN force estimator is shown in Fig. 6, 7, and in Table 3. In Fig. 6, the performance across a few random samples from the test set is shown. We can see that the range of the contact forces measured at each C_i varies. For this set of samples, the forces measured at the contact points closer to the base of the finger (C_1 and C_2) are mostly zeros. Non-zero forces are more commonly observed at C_i closer to the tip of the finger-exosuit system. Overall, we see that there is good agreement between the predicted and actual forces for this set of samples. Fig. 7 demonstrates the overall performance of the CNN force estimator across each C_i . Across all f_{C_i} in the test set, we see a moderate to strong correlation between the predicted and actual values. The violin plots show that the predicted values have a narrow distribution compared to the actual force values. The performance of the model was best for f_{C_2} and lowest for the f_{C_6} . C_2 and C_6 are respectively, the contact spheres at the bases of the second phalange and the fingertip (Fig. 1). The predicted and actual maximum contact forces for C_1 were 0.69 N and 2.41 N respectively. Similarly, for C_2 it was 1.43 N and 1.4 N, C_3 was 1.07 N and 3.7 N, C_4 was 0.95 N and 2.69 N, C_5 was 0.94 N and 1.67 N, C_6 was 0.28 N and 1.74 N, and C_7 was 0.11 N and 0.17 N respectively. The minimum value of the actual and predicted forces were 0 N for all f_{C_i} . Table 3 shows that the errors are generally quite small across C_i and are at worst 5.3% of the actual force values. The RMS% gets worse as C_i is closer to the tip, but the trend for CORR is not similar because of the variability in the range of forces measured at the contact points.

Table 4 demonstrates that the model is able to estimate the contact forces even though the contaminated images were not part of the training or validation routines. The model performs reasonably well even with medium gaussian noise (var = 0.01), and performs worse for higher than lower contrast images.

We proceed to test the CNN force estimator as a force sensor within a feedback controller (Fig. 4). The figure shows that for all F_t , the F_{net} measured by the CNN force estimator overlaps with the reference SoRoSim model estimates. Steady state was reached in 7, 5, and 14 steps for 0.25, 0.3, and 0.35 N respectively. For F_t of 0.35 N, the SoRoSim toolbox estimates steps with discrete changes in F_{net} , whereas, the CNN force estimations are smoother. The second plot in Fig. 8 shows the u used to actuate the exosuit. We see that the CNN force estimator was able to estimate the

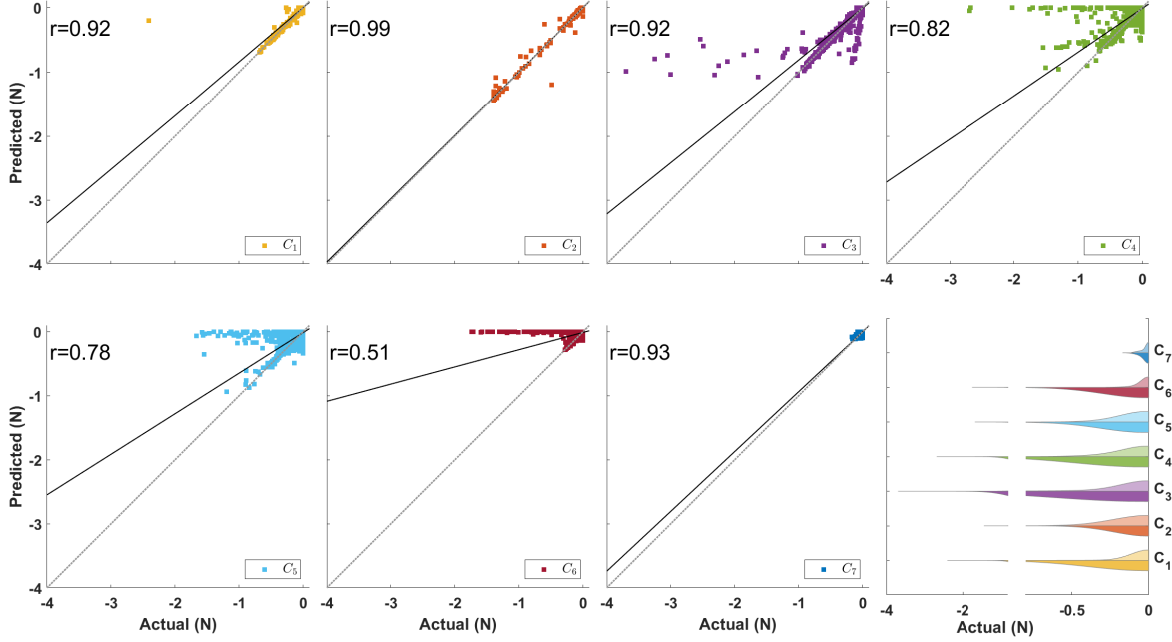


Figure 7: Overall performance of the CNN force estimator on the testing dataset. Each subplot shows the identity line and the correlation between predicted and actual forces for each C_i . The bottom right plot shows the raincloud distribution of the predicted (top half) versus actual (bottom half) force values.

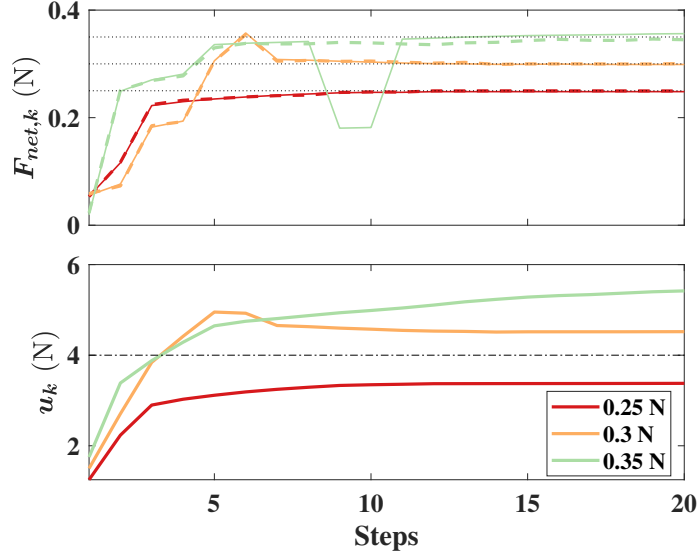


Figure 8: Steady-state responses of the feedback controller. In the top plot, the dotted lines denote F_{net} measured by the CNN force estimator, whereas the solid lines denote the reference from SoRoSim. The u_k is shown in the second plot. The black dotted line denotes the maximum actuation (4 N) used for generating the training datasets.

F_{net} even with poses where the exosuit actuation was greater than 4 N. This is noteworthy, since the training dataset did not include actuation beyond 4 N. We found that increasing the K_P reduced the steps needed to reach steady state for higher F_t , while worsening performance for lower F_t .

In Fig. 9, we show the step response of the feedback controller. The target $F_{t,k}$ is seen as black dotted lines in the first plot. K_P of 1 was best in tracking the step input and bringing the exosuit back to initial pose after the actuation is

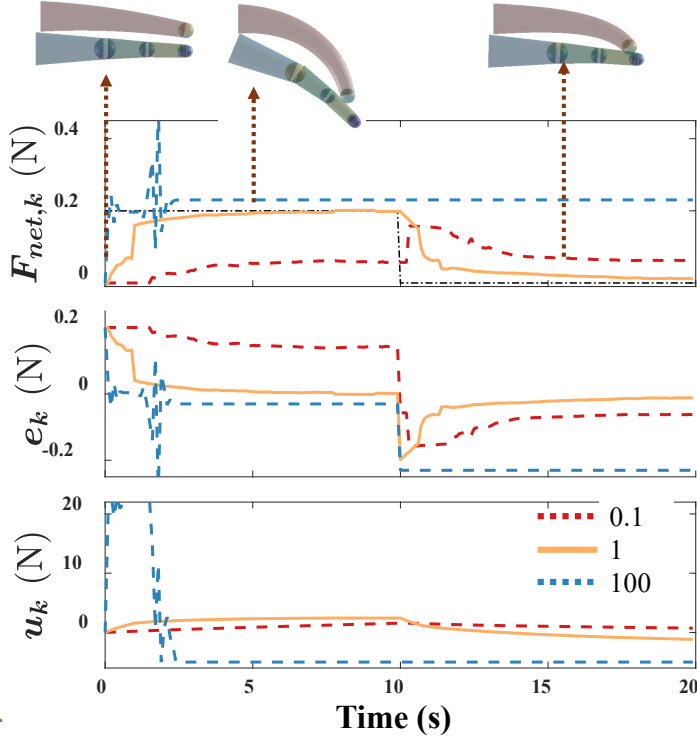


Figure 9: Step responses of the feedback controller. The first plot shows the measured F_{net} . The black dotted line denotes the target F_t . The second plot shows the error e , and the third plot shows the estimated u . The poses of the finger-exosuit system for $K_P = 1$ at different instances ($t = 0, 5, 10$ s) are shown at the top.

switched off. This is visible in the inset frames shown on top of the figure. The controller provides an u_k of 2.4 N for the exosuit to exert a F_{net} of 0.2 N on the finger. After the F_t switches to 0 N, the controller actuates the exosuit with -1 N to bend the exosuit in the opposite direction and prevent contact with the finger. With $K_P = 0.1$, the controller takes longer to track the step input. Here, we can see that the actuation reaches at most to 1.6 N before the step input is switched off. Finally, $K_P = 100$ results in actuation values that overshoot the F_t . The finger-exosuit system ends up in a pose that it cannot recover from, as can be seen as a constant F_{net} of 0.23 N after 2.6 s.

4 Discussion

This study highlights the feasibility of using image-based learning models to understand and predict human-exosuit interactions. Here, we demonstrated a CNN force estimator that mapped snapshots of finger-exosuit pose to interaction forces between them. SoRoSim toolbox [Mathew et al., 2024] was used for simulating a comprehensive dataset for training the CNN. To ensure generalizability, different formulations of the exosuit surface were utilized. The findings show that the methodology has potential for translation to real-world scenarios.

Fig. 7 and Table 3 show that the CNN force estimator was able to reproduce the interaction forces well. The RMS% (at most 5.3%) shows that the errors are small compared to the overall distribution. Generally, we see in Fig. 7 that the model predicts forces to be closer to zero compared to the distribution of the actual force values. The CNN was not good with mapping outlier force values either due to the lack of examples in the dataset or because of erroneous estimation by the simulation toolbox itself (such instances are observed at high force values).

The CNN-based force estimator was able to abstract sufficient information from the images to be generalizable (Table 4). Adding low or medium gaussian noise, or reducing image contrasts did not affect the performance of the model. However, deterioration of image quality (Fig. 3), and thereby features, reduced the performance. This was seen for very noisy or high contrast images.

We integrated the CNN model as a force sensor within a feedback controller. Irrespective of the target being tracked in Fig. 8, the CNN performance was similar to the reference SoRoSim values. Strikingly, the CNN force estimator was able to estimate the interaction forces when the exosuit was actuated beyond 4 N, even though these values were not

included in the training dataset. This suggests that the CNN was able to generalize a relationship between pose and net interaction force from the low-resolution grayscale images, and extrapolate to poses not included in the training dataset. Moreover, for higher actuation values, we observe benefits over SoRoSim estimation. For certain actuation values, the simulation platform measures a drop in interaction force erroneously, whereas, the CNN force estimator measures a continuously smooth change in the net force estimates.

Modelling the interface dynamics between assistive devices and human is necessary for designing efficient systems [Bardi et al., 2022]. Studies show that more than half of the assistive power can be lost in the soft interface between the exosuit and user [Yandell et al., 2017]. Increasing the stiffness of the interface further reduces the power available for joint assistance [Barrutia et al., 2024]. However, modelling the interaction forces is not trivial in real-world scenarios [Xiloyannis et al., 2019, Andrikopoulos et al., 2015]. Although, there have been studies using computer vision to predict interaction forces between humans (or soft-robots) and objects [Pham et al., 2018, Kennedy and Desai, 2005, Huang et al., 2024], they do not consider assistive devices. In this study, we demonstrate the potential of using images to predict interaction forces through a learning-based approach. Notably, our model exhibits strong generalization capabilities, successfully capturing interaction forces even when image quality is degraded. This suggests its applicability in real-world scenarios where camera data may be noisy or of low resolution. Furthermore, we show that the model can generalize to higher actuation forces that were not represented in the training data, indicating its robustness across a broader range of operating conditions. Finally, when integrated into a feedback control system, the model functions as a surrogate force sensor, offering a practical alternative to physical force sensing.

There are a few limitations to this study. The study offers insights only based on simulation trials, and translation to real-world scenarios and validating the findings is necessary to continue translation to actual practice. The current study modelled the finger-exosuit interface using a simple contact model with normal forces. Moreover, the system's static equilibrium was solved for each pose with increasing actuation for the exosuit. Tangential friction and velocity-dependent interactions could be included to improve the interaction force estimations [Flores, 2022, Ménager et al., 2025]. Additionally, we only simulated variations in the exosuit shape, with constant dimensions of the finger joint. Inclusion of different finger dimensions could improve the variability of the dataset. Future work will focus on extending the approach to multi-joint exosuits and incorporating real-world data to validate the model beyond simulated environments. Additionally, exploring reinforcement learning techniques to refine exosuit control strategies based on the learned interaction forces presents an exciting avenue for further research [Caggiano et al., 2022].

The study presents a robust, data-driven framework for modeling human-exosuit interfaces using simulation and deep learning. Its generalizability shows promise for real-world application, including low-resolution imaging scenarios, while sufficient training data may reduce reliance on precise interface modeling or force sensors.

Acknowledgment

This work was partly supported by the Netherlands Sectorplan Techniek 2 and the Royal Society research grants RGS/R1/231472 and IES/R2/242059. The authors thank Yunqi Huang for fabricating the exosuit, and Arvid Keemink for the training infrastructure.

References

Raymond J. Holt, Alexis S. Lefevre, Ian J. Flatters, Pete Culmer, Richard M. Wilkie, Brian W. Henson, Geoff P. Bingham, and Mark Mon-Williams. Grasping the changes seen in older adults when reaching for objects of varied texture. *PLoS ONE*, 8, 7 2013. ISSN 19326203. doi:10.1371/journal.pone.0069040.

M Saes, M. I. Mohamed Refai, B. J.F. van Beijnum, J. B.J. Bussmann, E P Jansma, P H Veltink, J H Buurke, E. E.H. van Wegen, C. G.M. Meskers, J W Krakauer, and G Kwakkel. Quantifying quality of reaching movements longitudinally post-stroke: A systematic review, 2022. ISSN 15526844.

Elena Bardi, Marta Gandolla, Francesco Braghin, Ferruccio Resta, Alessandra L.G. Pedrocchi, and Emilia Ambrosini. Upper limb soft robotic wearable devices: a systematic review. *Journal of NeuroEngineering and Rehabilitation*, 19, 12 2022. ISSN 17430003. doi:10.1186/s12984-022-01065-9.

David Scherb, Sandro Wartzack, and Jörg Miehling. Modelling the interaction between wearable assistive devices and digital human models—a systematic review. *Frontiers in Bioengineering and Biotechnology*, 10:1–11, 2023. ISSN 22964185. doi:10.3389/fbioe.2022.1044275.

Alan T. Asbeck, Stefano M.M. De Rossi, Ignacio Galiana, Ye Ding, and Conor J. Walsh. Stronger, smarter, softer: Next-generation wearable robots. *IEEE Robotics and Automation Magazine*, 21:22–33, 2014. ISSN 10709932. doi:10.1109/MRA.2014.2360283.

Daniela Rus and Michael T. Tolley. Design, fabrication and control of soft robots, 5 2015. ISSN 14764687.

Stefano Massardi, David Rodriguez-Cianca, David Pinto-Fernandez, Juan C. Moreno, Matteo Lancini, and Diego Torricelli. Characterization and evaluation of human–exoskeleton interaction dynamics: A review. *Sensors*, 22: 3993, 5 2022. ISSN 1424-8220. doi:10.3390/s22113993.

George Andrikopoulos, George Nikolakopoulos, and Stamatis Manesis. Motion control of a novel robotic wrist exoskeleton via pneumatic muscle actuators. In *IEEE International Conference on Emerging Technologies and Factory Automation, ETFA*, volume 2015-October. IEEE, 10 2015. ISBN 9781467379298. doi:10.1109/ETFA.2015.7301464.

Michele Xiloyannis, Domenico Chiaradia, Antonio Frisoli, and Lorenzo Masia. Characterisation of pressure distribution at the interface of a soft exosuit: Towards a more comfortable wear. In *Wearable Robotics: Challenges and Trends*, pages 35–38. Springer International Publishing, 2019. ISBN 978-3-030-01887-0.

Fouzia Khan, Roy J Roesthuis, and Sarthak Misra. Force sensing in continuum manipulators using fiber bragg grating sensors. In *2017 IEEE/RSJ International Conference on Intelligent Robots and Systems (IROS)*, pages 2531–2536. IEEE, 2017.

Hedan Bai, Shuo Li, Jose Barreiros, Yaqi Tu, Clifford R Pollock, and Robert F Shepherd. Stretchable distributed fiber-optic sensors. *Science*, 370(6518):848–852, 2020.

Yohan Noh, Joao Bimbo, Sina Sareh, Helge Wurdemann, Jan Fraš, Damith Suresh Chathuranga, Hongbin Liu, James Housden, Kaspar Althoefer, and Kawaal Rhode. Multi-axis force/torque sensor based on simply-supported beam and optoelectronics. *Sensors*, 16(11):1936, 2016.

Daisuke Haraguchi, Takahiro Kanno, Kotaro Tadano, and Kenji Kawashima. A pneumatically driven surgical manipulator with a flexible distal joint capable of force sensing. *IEEE/ASME Transactions on Mechatronics*, 20(6): 2950–2961, 2015.

David B Camarillo, Christopher F Milne, Christopher R Carlson, Michael R Zinn, and J Kenneth Salisbury. Mechanics modeling of tendon-driven continuum manipulators. *IEEE transactions on robotics*, 24(6):1262–1273, 2008.

Anzhu Gao, Ryan J Murphy, Hao Liu, Iulian I Iordachita, and Mehran Armand. Mechanical model of dexterous continuum manipulators with compliant joints and tendon/external force interactions. *IEEE/ASME Transactions on Mechatronics*, 22(1):465–475, 2016.

D. Caleb Rucker and Robert J. Webster. Deflection-based force sensing for continuum robots: A probabilistic approach. In *2011 IEEE/RSJ International Conference on Intelligent Robots and Systems*, 2011. doi:10.1109/IROS.2011.6094526.

Andrea Bajo and Nabil Simaan. Hybrid motion/force control of multi-backbone continuum robots. *The International journal of robotics research*, 35(4):422–434, 2016.

François Faure, Christian Duriez, Hervé Delingette, Jérémie Allard, Benjamin Gilles, Stéphanie Marchesseau, Hugo Talbot, Hadrien Courtecuisse, Guillaume Bousquet, Igor Peterlik, and Stéphane Cotin. *SOFA: A Multi-Model Framework for Interactive Physical Simulation*, pages 283–321. Springer Berlin Heidelberg, Berlin, Heidelberg, 2012. ISBN 978-3-642-29014-5. doi:10.1007/978-3-642-29014-5_12.

Etienne Ménager, Louis Montaut, Quentin Le Lidec, and Justin Carpentier. Differentiable simulation of soft robots with frictional contacts. 1 2025. URL <http://arxiv.org/abs/2501.18956>.

Cosimo Della Santina, Christian Duriez, and Daniela Rus. Model-based control of soft robots: A survey of the state of the art and open challenges. *IEEE Control Systems*, pages 30–65, 6 2023. ISSN 1066-033X. doi:10.1109/MCS.2023.3253419.

Costanza Armanini, Frederic Boyer, Anup Teejo Mathew, Christian Duriez, and Federico Renda. Soft robots modeling: A structured overview. *IEEE Transactions on Robotics*, 39:1728–1748, 2023. ISSN 19410468. doi:10.1109/TRO.2022.3231360.

Anup Teejo Mathew, Ikhlas Ben Hmida, Costanza Armanini, Frederic Boyer, and Federico Renda. Sorosim: A matlab toolbox for hybrid rigid-soft robots based on the geometric variable-strain approach. *IEEE Robotics and Automation Magazine*, 30:106–122, 2023. ISSN 1558223X. doi:10.1109/MRA.2022.3202488.

F. Boyer, V. Lebastard, F. Candelier, and F. Renda. Dynamics of continuum and soft robots: A strain parameterization based approach. *IEEE Transactions on Robotics*, pages 1–17, 2020. doi:10.1109/TRO.2020.3036618.

Federico Renda, Costanza Armanini, Vincent Lebastard, Fabien Candelier, and Frederic Boyer. A geometric variable-strain approach for static modeling of soft manipulators with tendon and fluidic actuation. *IEEE Robotics and Automation Letters*, 5(3):4006–4013, 2020.

Anup Teejo Mathew, Daniel Feliu-Talegon, Abdulaziz Y Alkayas, Frederic Boyer, and Federico Renda. Reduced order modeling of hybrid soft-rigid robots using global, local, and state-dependent strain parameterization. *The International Journal of Robotics Research*, pages 1–26, 2024. doi:10.1177/02783649241262333.

Richard Marques Monteiro, Helge Wurdemann, Richard Marques Monteiro, Jialei Shi, Helge Wurdemann, Fumiya Iida, and Thomas George Thuruthel. Visuo-dynamic self-modelling of soft robotic systems. pages 0–27, 2023. doi:<https://doi.org/10.21203/rs.3.rs-3626336/v1>.

Xingyu Chen, Jialei Shi, Helge Wurdemann, and Thomas George Thuruthel. Vision-based tip force estimation on a soft continuum robot. In *2024 IEEE International Conference on Robotics and Automation (ICRA)*, pages 7621–7627. IEEE, 2024.

Yunqi Huang, Abdulaziz Y. Alkayas, Jialei Shi, Federico Renda, Helge Wurdemann, and Thomas George Thuruthel. Predicting interaction shape of soft continuum robots using deep visual models. In *2024 IEEE/RSJ International Conference on Intelligent Robots and Systems (IROS)*, pages 11381–11387, 10 2024. ISBN 979-8-3503-7770-5. doi:10.1109/IROS58592.2024.10801261.

Federico Renda, Costanza Armanini, Anup Mathew, and Frederic Boyer. Geometrically-exact inverse kinematic control of soft manipulators with general threadlike actuators’ routing. *IEEE Robotics and Automation Letters*, 7 (3):7311–7318, 2022. doi:10.1109/LRA.2022.3183248.

Pei Hsin Kuo and Ashish D. Deshpande. Muscle-tendon units provide limited contributions to the passive stiffness of the index finger metacarpophalangeal joint. *Journal of Biomechanics*, 45, 10 2012. ISSN 00219290. doi:10.1016/j.jbiomech.2012.07.034.

Xiang Qian Shi, Ho Lam Heung, Zhi Qiang Tang, Kai Yu Tong, and Zheng Li. Verification of finger joint stiffness estimation method with soft robotic actuator. *Frontiers in Bioengineering and Biotechnology*, 8, 12 2020. ISSN 22964185. doi:10.3389/fbioe.2020.592637.

Kevin M. Lynch and Frank C. Park. *Modern Robotics: Mechanics, Planning, and Control*. Cambridge University Press, 2017.

Bastian Bechtold. Violin plots for matlab, 2016. URL <https://github.com/bastibe/Violinplot-Matlab>.

Matthew B. Yandell, Brendan T. Quinlivan, Dmitry Popov, Conor Walsh, and Karl E. Zelik. Physical interface dynamics alter how robotic exosuits augment human movement: implications for optimizing wearable assistive devices. *Journal of NeuroEngineering and Rehabilitation*, 14, 2017. ISSN 17430003. doi:10.1186/s12984-017-0247-9.

W. Sebastian Barrutia, Ada Yumiceva, Mai-Ly Thompson, and Daniel P. Ferris. Soft tissue can absorb surprising amounts of energy during knee exoskeleton use. *Journal of The Royal Society Interface*, 21, 12 2024. ISSN 1742-5662. doi:10.1098/rsif.2024.0539.

Tu Hoa Pham, Nikolaos Kyriazis, Antonis A. Argyros, and Abderrahmane Kheddar. Hand-object contact force estimation from markerless visual tracking. *IEEE Transactions on Pattern Analysis and Machine Intelligence*, 40: 2883–2896, 12 2018. ISSN 19393539. doi:10.1109/TPAMI.2017.2759736.

C. W. Kennedy and J. P. Desai. A vision-based approach for estimating contact forces: Applications to robot-assisted surgery. *Applied Bionics and Biomechanics*, 2:53–60, 1 2005. ISSN 1176-2322. doi:10.1533/abbi.2004.0006.

Paulo Flores. Contact mechanics for dynamical systems: a comprehensive review, 2 2022. ISSN 1573272X.

Vittorio Caggiano, Huawei Wang, Guillaume Durandau, Massimo Sartori, and Vikash Kumar. Myosuite – a contact-rich simulation suite for musculoskeletal motor control. 2022. URL <http://arxiv.org/abs/2205.13600>.